



Inherent vacancy of compressive Ru nanoparticles accelerate electro-catalytic hydrogen energy conversion

Qikang Wu^a, Wenjuan Yang^{b,*}, Xingdong Wang^c, Wei Zhu^{c,*}, Shanshan Lv^a, Yan Zhou^a, Taiyu Chen^a, Shaohuan Liu^a, Wanying Li^a, Zheng Chen^{a,d,**}

^a Key Laboratory of Functional Molecular Solids, Ministry of Education, Anhui Key Laboratory of Molecule-Based Materials, College of Chemistry and Materials Science, Anhui Normal University, Wuhu 241002, PR China

^b Julong College, Shenzhen Technology University, Shenzhen 518118, PR China

^c State Key Lab of Organic-Inorganic Composites, Beijing University of Chemical Technology, Beijing 100029, PR China

^d State Key Laboratory of Coordination Chemistry, Nanjing University, Nanjing 210023, PR China

ARTICLE INFO

Keywords:

HER
HOR
Defective structure
Lattice strain
Ru nanoparticles

ABSTRACT

Single factor such as defect or strain is adopted to regulate Ru-based catalysts for HER and HOR, which usually fail to accurately describe the complex catalysis. Herein, ultrafine Ru nanoparticles with vacancies and compressive stress are formed on carbon (V-S-Ru/C) as revealed by electronic and spectroscopic characterizations. This V-S-Ru/C has excellent HER activity with a low overpotential of 21 mV to deliver 10 mA/cm², and the mass activity is 35.6 times that of commercial Pt/C at 100 mV overpotential. The V-S-Ru/C could also achieve 7.2 times mass activity of commercial Pt/C for HOR and has oxidation resistance in high potential range. The V-S-Ru/C shows lower barrier of rate-determining step, because the defect and strain synergistically induce the upshift of d-band center on Ru to promote the adsorption of key intermediates based on theoretical calculation. The cooperative regulation of defect and strain provide a new pathway for mechanism insight and designing catalyst.

1. Introduction

Due to its high energy density and energy conversion efficiency, hydrogen is expected to replace traditional fossil energy sources that face depletion and combustion pollution [1–5]. As two important reactions of hydrogen energy conversion, the electrochemical hydrogen evolution reaction (HER) and hydrogen oxidation reaction (HOR) need robust catalysts to overcome the slow kinetic process, to improve the efficiency of hydrogen energy conversion [3,6–9]. Pt has limited its widespread use because of its high price and scarcity [10,11]. Meanwhile, the requirements for equipment under acidic conditions are more stringent than those under alkaline conditions [12–15]. In alkaline medium, electrochemical HER principally involves three reactions on the surface of a catalyst [16,17]. The first step is commonly the Volmer step ($\text{H}_2\text{O} + \text{e}^- + \text{Cat} \rightleftharpoons \text{Cat-H}_{\text{ad}} + \text{OH}^-$, Cat-H_{ad} represents the active hydrogen adsorbed on the catalyst surface), which is followed by either the Tafel step ($\text{Cat-H}_{\text{ad}} + \text{Cat-H}_{\text{ad}} \rightleftharpoons 2\text{Cat} + \text{H}_2$) or Heyrovsky step

($\text{Cat-H}_{\text{ad}} + \text{e}^- + \text{H}_2\text{O} \rightleftharpoons \text{Cat} + \text{H}_2 + \text{OH}^-$) to give H₂. While for the HOR in the alkaline medium, H₂ molecule firstly dissociates with the formation of Cat-H_{ad} via either a Heyrovsky step or a Tafel step and then undergoes a Volmer step [18]. Unlike in an acidic medium, the HER or HOR activity of catalysts in basic medium deviates from the typical Sabatier principle based on active hydrogen descriptor merely [19–21]. Because the Volmer process requires additional energy to decompose or form water to generate active hydrogen [20,22,23], the HER or HOR activity of Pt-based catalysts in alkaline medium is much lower than that in an acidic medium [24–26].

The development of Ru-based HER catalysts has attracted great attention because Ru has a similar H-binding ability to Pt, and its price is much lower than Pt [25,27–29]. To further improve the catalytic activity of Ru and reduce its usage of Ru, many useful synthetic strategies have been proposed including metal support interaction, ligand modification, alloying, doping, and atomization [5,22,30–39]. Among many synthetic strategies, the preparation of uniformly loaded Ru

* Corresponding authors.

** Corresponding author at: Key Laboratory of Functional Molecular Solids, Ministry of Education, Anhui Key Laboratory of Molecule-Based Materials, College of Chemistry and Materials Science, Anhui Normal University, Wuhu 241002, PR China.

E-mail addresses: ywj914315@163.com (W. Yang), zhuwei@mail.buct.edu.cn (W. Zhu), chenzh07@mail.ahnu.edu.cn (Z. Chen).

<https://doi.org/10.1016/j.apcatb.2023.122896>

Received 9 March 2023; Received in revised form 27 April 2023; Accepted 18 May 2023

Available online 19 May 2023

0926-3373/© 2023 Elsevier B.V. All rights reserved.

nanoparticles using carbon-based supports has attracted much attention due to their excellent electrical conductivity, structural diversity and modifiability [40–43]. It is reported that the interaction between Ru nanoparticles and nitrogen-doped carbon is conducive to enhancing catalytic activity in HER due to the formation of the Schottky junction and lattice stress [44]. Although many works of carbon-supported Ru nanoparticles with excellent performance have been reported, the complex synthetic procedures and the high loading of ruthenium make these works difficult to face practical applications [11,30,35,45]. The development of Ru-based HOR catalysts lags far behind HER, because the OH* with strong oxidation and its strong H* absorption capacity in HOR are easy to cause the loss of active sites [46–50]. The intrinsic activity of Ru nanoparticles could be improved through optimize the hydrogen binding energy (HBE) with adjustment of size, support and doping. The defect engineering of Ru by decreasing in size of nanoparticles could effectively lower the activation energy for both H* absorption and H₂O desorption, thus improving the catalytic activity of HOR [51]. The optimization of the support is helpful to enhance the interaction with metallic species such as Ru nanoparticles partially confined in the lattice of TiO₂, and resulting in the charge redistribution between the Ru nanoparticles and support [52]. The introduction of heteroatoms on the surface of Ru nanoparticles can effectively adjust the electronic structure of Ru, thus optimizing the adsorption of H* and improving the HOR of Ru sites [28]. The regulation means (such as defect engineering and strain engineering) of electronic structure or band structure of Ru are separate, and the cooperative regulation of defect and strain is rarely studied but instrumental in understanding the mechanism and mining activity in real catalysis. In addition to the HBE theory, another OH binding energy (OHBE) theory has been also proposed to mediate the activity of HOR catalysts under alkaline conditions [3,53,54]. The RuMo alloy prepared by introducing oxygenophilic Mo atoms into hcp Ru nanoparticles can effectively mediate the binding energy of OHBE, thus showing higher HOR properties than pure hcp Ru nanoparticles [55]. Interestingly, H spillover from Ru surface can also be accelerated by introducing atomically dispersed chromium coordinated with hydroxyl clusters enabling efficient hydrogen oxidation on Ru nanoparticles [56].

Herein, ultrafine Ru nanoparticles supported on carbon are prepared at gram scale (2.4 g of one batch) by using acetylene black (AB), polyvinylpyrrolidone (PVP) and ruthenium complex as raw materials through mixing and annealing (V-S-Ru/C). It is shown that 2–3 nm Ru nanoparticles with lattice distortion and vacancy were uniformly dispersed on a twisted graphitized carbon layer which is produced by calcination at high temperatures. X-ray absorption fine structure (XAFS) characterization and its analysis show that the formed Ru nanoparticles have lower coordination, which may be caused by the inherent vacancies. In the carbon-supported Ru nanoparticle with lattice stress catalyst (S-Ru/C) prepared without PVP, the size of Ru is large (> 5 nm) and some particles are agglomerated. BET results show that V-S-Ru/C (142.454 m²/g) has a slightly larger specific surface area than S-Ru/C (90.095 m²/g), while ICP-OES results show that they have similar Ru content (~0.8 wt%). When applied to HER, the V-S-Ru/C catalyst shows a low Tafel slope of 31.08 mV/dec and overpotential of 21 mV (at 10 mA/cm², η_{10}), significantly better than S-Ru/C, and commercial 20 wt% Pt/C. Compared with the S-Ru/C catalyst, the V-S-Ru/C catalyst has a smaller particle size, larger electrochemical active area, higher mass activity and optimize surface H_{ad} adsorption. HOR test results show that compared with the S-Ru/C, the V-S-Ru/C catalyst has high apparent activity and mass activity.

2. Experiment part

2.1. Synthesis of V-S-Ru/C

Add 2 g PVP and 100 mL H₂O into a 1000 mL flask. After stirring for 10 min (min), 2 g AB and 100 mL ethanol were added into the above

flask. 405 mg Ru(acac)₃ was added after 30 min of ultrasound. The mixture was subjected to ultrasound for 20 min, stir overnight and rotary evaporation to obtain a black mixture (4.21 g). The V-S-Ru/C catalyst can be obtained by fully grinding the black mixture and two stages of calcination. The temperature of the high-temperature section was controlled at 800 °C, and the temperature of the low-temperature section was optimized (200, 300, 400 °C). In addition, one-step direct calcination at 800 °C was also done for comparison.

2.2. Characterization

Scanning electron microscopy (SEM) images and Transmission electron microscopy (TEM) images were captured by using Hitachi S8100 SEM and Hitachi HT-7700 respectively. High-resolution transmission electron microscopy (HRTEM) and High-angle annular dark-field scanning transmission electron microscopy (HAADF-STEM) were obtained from JEOL JEM 2100 F. Aberration-corrected High-angle annular dark-field scanning transmission electron microscopy (AC-HAADF-STEM) was obtained from JEOL JEM 2100 F Titan Cubed Themis G2300. The Brunauer-Emmet-Teller (BET) surface area was measured by JW-BK200C. An inductively Coupled Plasma-Optical Emission Spectrometer (ICP-OES) was utilized to determine the Ru content of catalysts (Aglient 5110). The powder X-ray diffraction (XRD) was performed by a Smartlab 9 kb equipped with Cu-K α radiation source. X-ray photoelectron spectroscopy (XPS) was conducted on a Thermo Scientific K-Alpha instrument with Al-K α as a monochromatic X-ray source. X-ray absorption fine structure (XAFS) spectroscopy was carried out using the RapidXAFS HE Ultra (Anhui Absorption Spectroscopy Analysis Instrument Co., Ltd.) by transmission mode at 40 kV and 45 mA, and the Si (12 12 8) spherically bent crystal analyzer with a radius of curvature of 500 mm was used for Ru.

2.3. Electrochemical measurements

For HER, all electrochemical measurements were conducted on an electrochemical workstation (CHI 660E) with a conventional three-electrode electrochemical cell, an Hg/HgO (1 M KOH) electrode, a graphite and catalyst-modified glassy carbon electrode (GCE) were used as the reference electrode, the counter electrode and the working electrode, respectively. To prepare the working electrodes, typically, 5 mg of catalyst and 10 μ L Nafion solution are added to a mixture of 500 mL ethanol and 500 mL deionized water, and sonically dispersed for 0.5 h to form a uniform ink, the glassy carbon electrode (GCE, 0.07065 cm² in surface) was pre-polished with a 50 nm alumina powder, apply 8 μ L of ink onto the GCE surface using a pipette and then dried naturally, the catalyst's mass was ~0.566 mg/cm² (The same method was also used to prepare Pt/C modified GCE electrodes). The frequency range of electrochemical impedance spectroscopy (EIS) was 10⁵ Hz~0.01 Hz (tested at 53 mV overpotential). The double-layer capacitances (C_{dl}) were obtained by cyclic voltammetry (CV) test at different sweep rates and the voltage window is from 0.117 V to 0.217 V (vs. RHE, reversible hydrogen electrode). Electrochemical active surface area (ECSA) values were calculated using the following equation, ECSA= C_{dl}/C_s , where, C_s refers to the specific capacitance of a flat surface and from the previous literature we have used the value of C_s as 0.040 mF/cm². The linear sweep voltammetry (LSV) was tested at a scan rate of 5.0 mV/s. The stability of the samples was evaluated by chronopotentiometry (CP) at a current density of 10 mA/cm² and CV was performed at a scan rate of 100 mV/s respectively. The potential, measured against an Hg/HgO electrode in 1 M KOH, was converted to the potential versus the RHE according to E (vs. RHE) = E (vs. Hg/HgO) + 0.917 V.

The HOR test of the catalyst was carried out in 0.1 M KOH saturated with hydrogen (supplied by high-purity hydrogen generator). If the preparation method and loading of catalyst-modified GCE are not specified, the reference electrode and counter electrode are the same as the HER test. LSV was tested at a scan rate of 10 mV/s. The stability of

the catalysts was evaluated by CV methods at a scan rate of 100 mV/s. In addition, the V-S-Ru/C catalyst was further loaded onto carbon paper (1 cm × 1 cm, mass loading: 1 mg/cm²) to further test the stability of the catalyst. The potential, measured against an Hg/HgO electrode in 0.1 M KOH, was converted to the potential versus the RHE according to $E \text{ (vs. RHE)} = E \text{ (vs. Hg/HgO)} + 0.866 \text{ V}$.

HEMFC assembly: Catalyst ink was obtained by mixing the powdered catalyst with 5 wt% Nafion ionomers (D520) diluted by isopropanol/water with a volume ratio of 25:1. This ink was ultrasonically treated for 2 h at 0 °C and sprayed on two sides of Versogen membrane (an active area of 5 cm²). V-S-Ru/C with a loading of 0.2 mg_{Ru}/cm², while 40 wt% Pt/C was used as a cathodic catalyst with a loading of 0.4 mg_{Pt}/cm². The catalyst-coated membrane and gas diffusion layer was assembled in a standard test cell of 5.0625-cm² fixture. Then, we tested them using Scribner 850e as a condition-controlled fuel cell test station. The fuel cell polarization curve was recorded at 80 °C and 100% relative humidity. For hydrogen supply and oxygen supply, the back pressures were fixed at 200 kPa, and gas flow rates were fixed at 500 mL/min.

2.4. Computational method

Density functional theory (DFT), as implemented in the Vienna ab initio simulation program (VASP), served as the foundation for all theoretical computations. In the Perdew-Burke-Ernzerhof functional (GGA-PBE), the electron exchange and correlation energy were handled inside the generalized gradient approximation [57]. With cutoff energies of 400 eV, plane-wave basis sets were used to characterize the valence orbitals [58]. With a (2 × 2 × 1) mesh, the Monkhorst-Pack technique was used to produce the k-point sampling. The conjugate

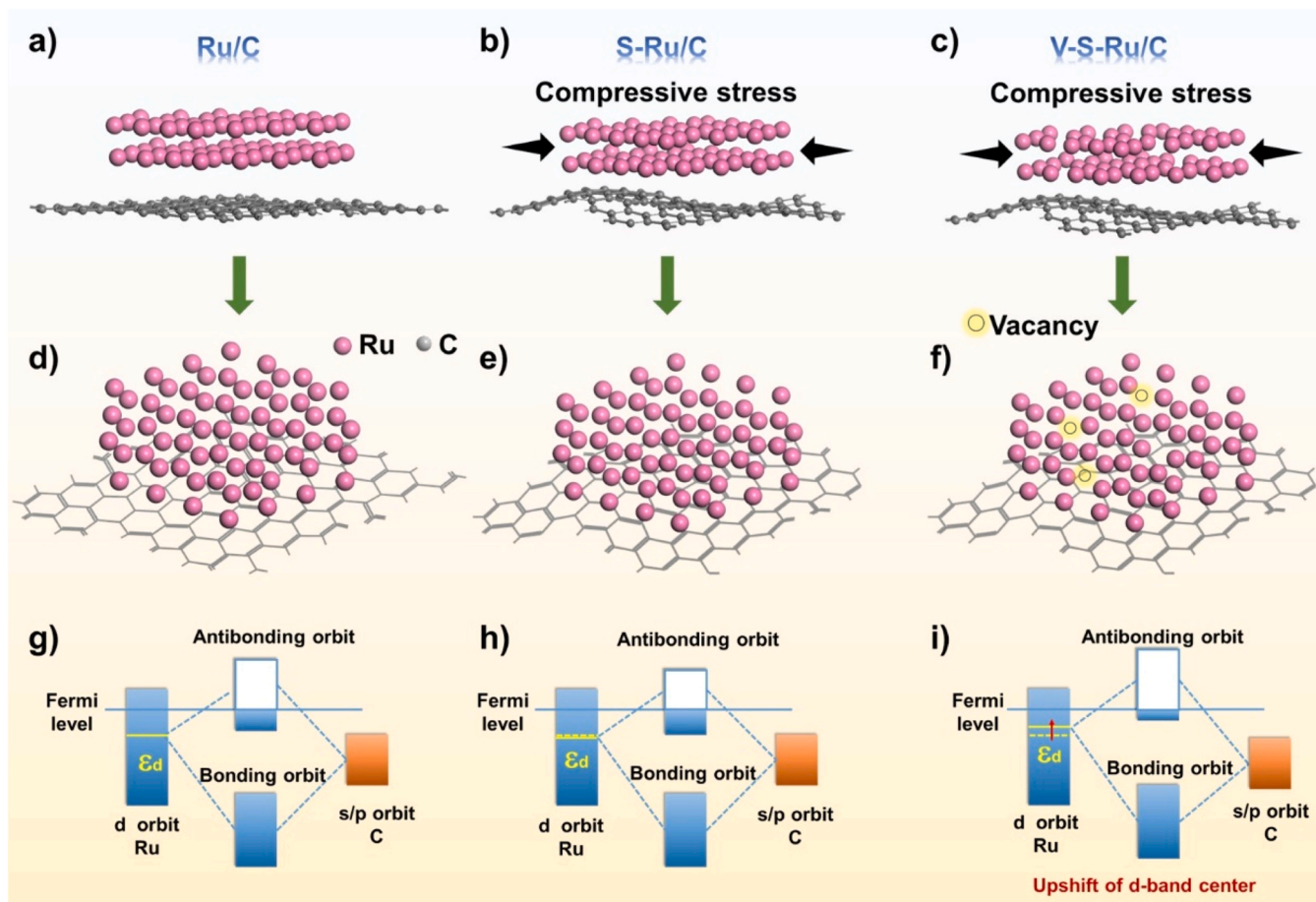
gradient approach completely relaxes the atomic coordinates (CG). The electronic self-consistent iteration and force convergence requirements were set to 10⁻⁴ eV and 0.02 eV, respectively.

The (H⁺ + e⁻) pair is transferred from the adsorbed species on the surface to the electrolyte in each stage of the electrochemical reaction in HER and HOR. The free energy change of each (H⁺ + e⁻) pair transfer reaction was calculated using the computational hydrogen electrode (CHE) approach developed by Nørskov et al. At standard condition (U = 0, pH = 0, p = 1 bar, T = 298 K), the free energy ΔG_0 of the reaction $^*AH \rightarrow A + H^+ + e^-$, can be calculated as the free energy of the reaction $^*AH \rightarrow A + 1/2 H_2$. $\Delta G_0 = \Delta E + \Delta ZPE + \Delta_{0 \rightarrow 298 K} \Delta H - T\Delta S$, is calculated as follows: The reaction energy $\Delta E = E(\text{product}) - E(\text{reactant})$. ΔZPE , ΔH and ΔS denote the difference in zero-point energy, enthalpy, and entropy due to the reaction, respectively. The enthalpy and entropy of the ideal gas molecule were taken from the standard thermodynamic Tables. Therefore, reaction free energy can be calculated by the equation: $\Delta G(U, \text{pH}, p = 1 \text{ bar}, T = 298 \text{ K}) = \Delta G_0 + \Delta G_{\text{pH}} + \Delta G_U$, where ΔG_{pH} is the correction of the free energy of H⁺ ions at a pH different from 0: $\Delta G_{\text{pH}} = -kT \ln[H^+] = kT \ln 10 \times \text{pH}$. $\Delta G_U = -eU$, where U is the electrode potential relative to the standard hydrogen electrode.

3. Results and discussion

3.1. The upshift of d-band center caused by defect engineering and stress engineering for Ru/C

Scheme 1 shows the different types of catalyst models designed in this study. The effect of vacancies and lattice stress on the HER/HOR activity of Ru nanoparticles was studied. The common Ru/C catalyst can



Scheme 1. Model diagrams of different Ru-based catalysts: a, b and c) cross-view of Ru/C, S-Ru/C and V-S-Ru/C; d, e and f) top-view of Ru/C, S-Ru/C and V-S-Ru/C respectively; The illustration of d band center shift of g) Ru/C, h) S-Ru/C and i) V-S-Ru/C.

be easily obtained by impregnation method on carbon. The particle size of this Ru/C catalyst is large, and there is no obvious vacancy (Scheme 1a and d). Since the interaction between Ru and carbon is not strong, there is no stress on Ru particles. The second catalyst is calcined at 300 °C firstly and then 800 °C of loading the Ru complex on the carbon. The particle size is large and there is no obvious vacancy. However, due to the calcination at high temperature, the interaction between the Ru nanoparticles and the support is enhanced, and twisted graphitized carbon layer also produces the compressive stress on the Ru particles (Scheme 1b and e). The third catalyst is obtained by calcining Ru complex protected by PVP on AB at high temperature. It has significantly smaller and uniform size, so it has more vacancies. Due to

high temperature treatment, the twisted surface graphite layer also produces obvious compressive stress on Ru particles (Scheme 1c and f). Through DFT calculation, it is found that the d-band center of S-Ru/C has a very slight downshift after the twisted graphitized carbon layer applied the compression stress on Ru nanoparticles. When there are vacancies on Ru nanoparticles with compressive stress, the d-band center will obviously occur upshift (Scheme 1i). The adjustment of d-band center will promote the adsorption of intermediate active species in the process of HER and HOR, thus showing excellent catalytic performance.

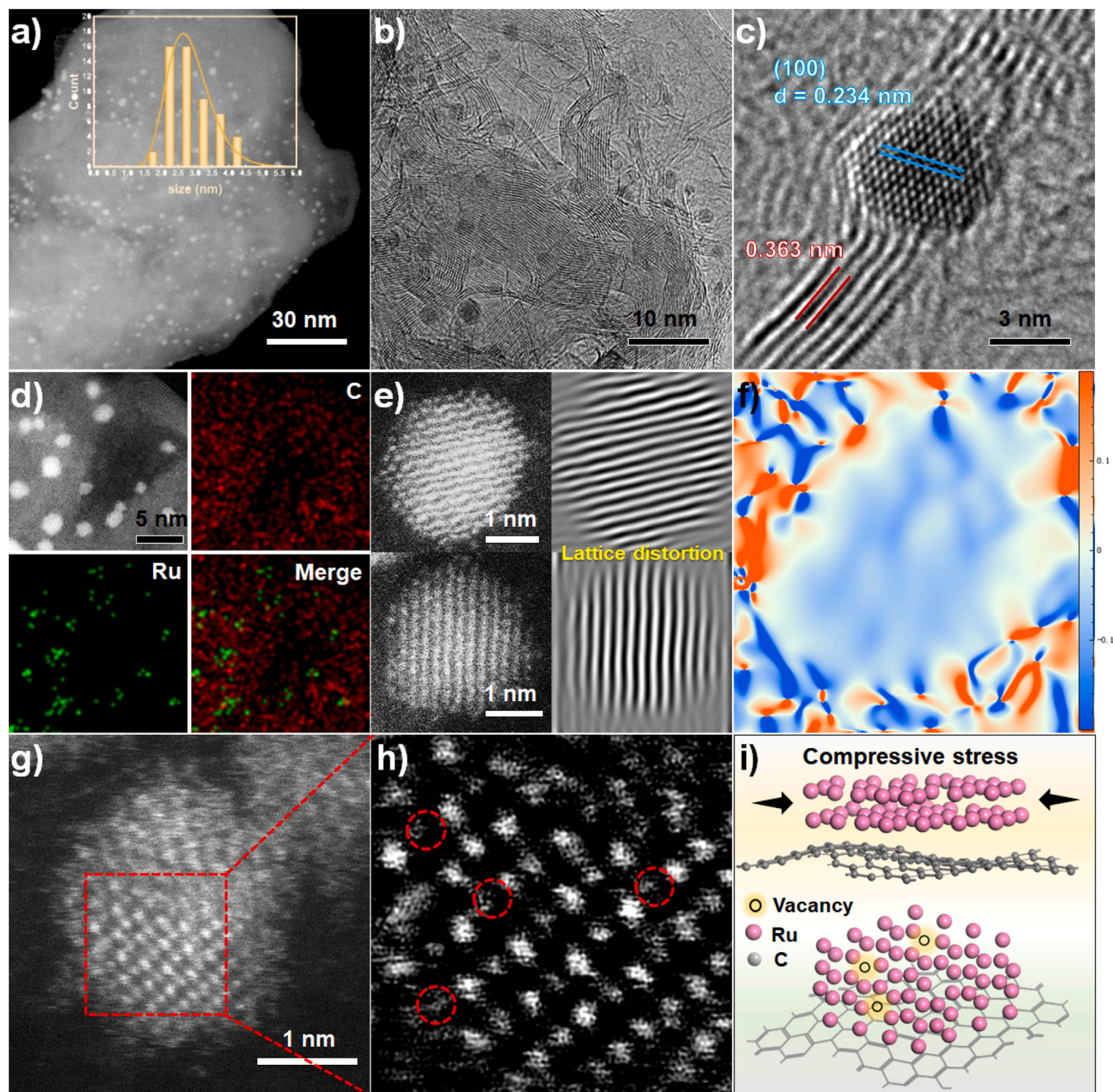


Fig. 1. (a) HAADF-STEM image of V-S-Ru/C (inset: diameter distribution of Ru nanoparticles in Ru-based catalysts); Both (b) and (c) are HRTEM images of V-S-Ru/C with different resolutions; (d) AC-HAADF-STEM image and corresponding EDS mappings of V-S-Ru/C; (e) AC-HAADF-STEM image and corresponding IFFT patterns in the AC-HAADF-STEM image; (f) ϵ_{yy} strain component determined via GPA of V-S-Ru/C; (g) AC-HAADF-STEM image and (h) enlarged part in (g); (i) constructed V-S-Ru/C model based on electron analysis results.

3.2. Synthesis and characterization of V-S-Ru/C catalyst

The morphology of carbon-based Ru catalysts were observed by transmission electron microscope (TEM, Fig. S1). By comparing Fig. S2a and b, it can be found that in the same synthetic process (first 300 °C and second 800 °C), the presence of PVP results in smaller size and uniform distribution of Ru nanoparticles loaded on carbon supports. The V-S-Ru/C catalysts with optimization at different low-temperature sections are similar, which are also alike to the direct one-step calcination results of 800 °C in the presence of PVP (Fig. S1b). If no special explanation was given later in this paper, the low temperature and high temperature of the synthesized V-S-Ru/C catalyst was 300 °C and 800 °C respectively. In addition, by comparing pure AB and S-Ru/C materials (Fig. S1a and f), it can be found that all the V-S-Ru/C catalysts synthesized with PVP have flexible carbon nanosheet structures, which can be attributed to the high-temperature carbonization of PVP. This is also consistent with the results of the ICP-OES, which detected that the content of Ru in V-S-Ru/C (0.7427 wt%) was lower than that in S-Ru/C (0.8292 wt%). From High-Resolution Transmission Electron Microscopy (HRTEM) images (Fig. 1a and b), it can be observed that the distribution of Ru nanoparticles in V-S-Ru/C is relatively uniform and the size is small (2.0–3.0 nm). However, the size of Ru nanoparticles in S-Ru/C

synthesized without PVP in Fig. S2d is larger (around 5.5 nm). The spacing of adjacent fringes is mainly 0.203, 0.213 and 0.234 nm (Figs. 1c and S2e), which is indexed to the (101), (002), and (100) crystalline plane of hexagonal close-packed (hcp) of Ru nanoparticles in V-S-Ru/C. Similar results were also observed in S-Ru/C (Fig. S2f). Elemental mapping analysis demonstrated that the Ru element is only distributed in nanoparticles, and no obvious Ru element is found in other parts of the carbon support. (Fig. 1d) Moreover, the corresponding inverse fast Fourier transform (IFFT) images were transformed based on the aberration-corrected high-angle annular dark-field scanning transmission electron microscopy (AC-HAADF-STEM) image, clearly indicating some of the local lattice distortion structure in some Ru nanoparticles (Fig. 1e), which may due to the defective structure or lattice stress [51]. The geometric phase analysis (GPA) was executed for investigating the effect of the carbon support on the lattice-strained Ru nanoparticles. The ϵ_{xx} and ϵ_{yy} components of the strain tensor exhibited more compression in the inner part of the nanoparticle than in the outer part, indicating that the Ru nanoparticles anchored on the carbon support were subjected to compressive stress (Fig. 1f and S3). From the enlarged part of Fig. 1g, it can be observed that the surface of Ru nanoparticles has some vacancies (Fig. 1h). Based on the above electron microscope analysis results, the structure model of the V-S-Ru/C catalyst

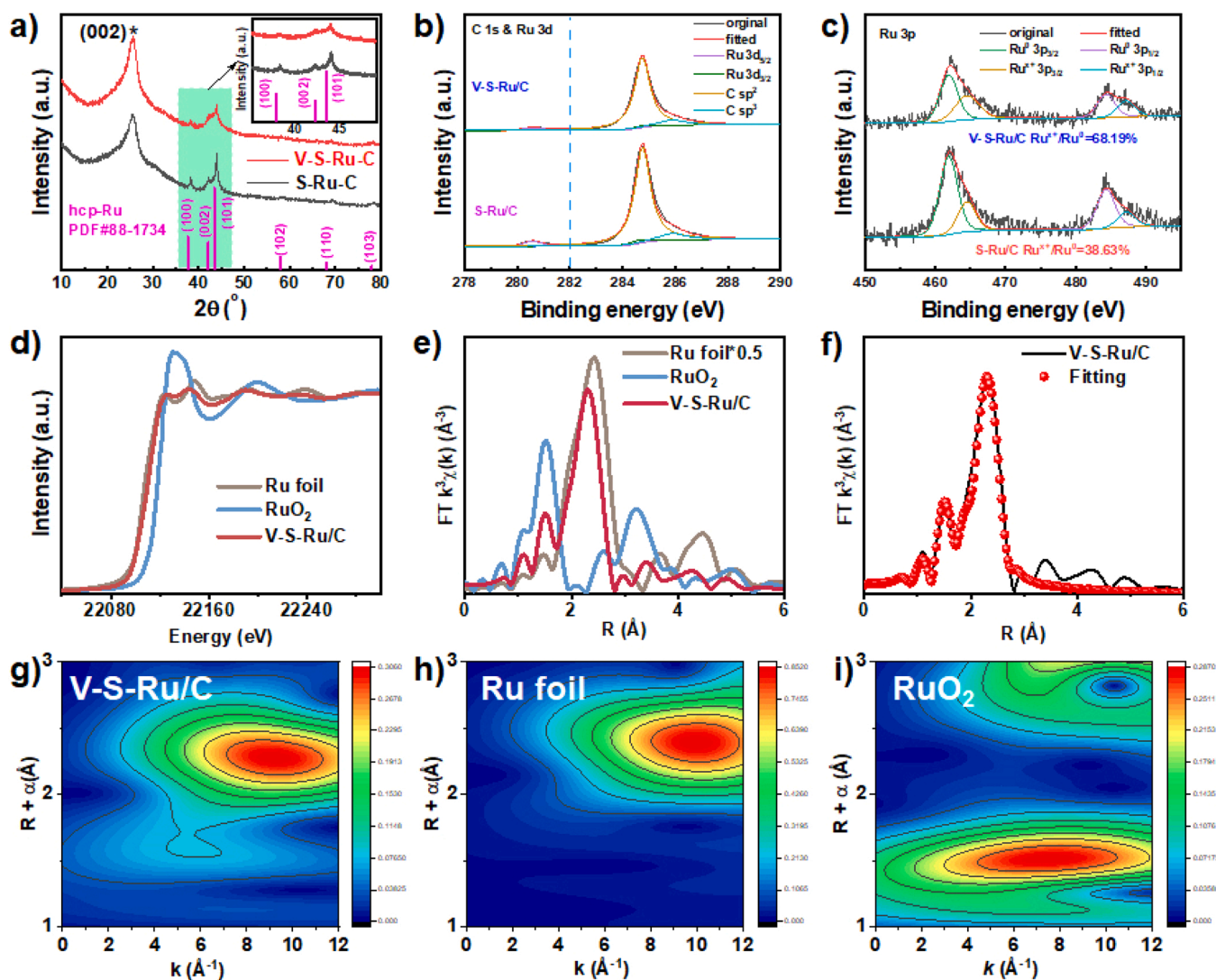


Fig. 2. (a) XRD patterns of Ru-based catalysts, and the inset is the enlarged image of selected area; The core-level XPS spectra of the (b) C1s & Ru 3d and (c) Ru 3p; (d) normalized XANES spectra at the Ru K-edge and (e) FT-EXAFS spectra at the R space of V-S-Ru/C, RuO₂, and Ru foil; (f) corresponding EXAFS R-space fitting curves of V-S-Ru/C. WT-EXAFS spectra of (g) V-S-Ru/C, (h) Ru foil, and (i) RuO₂, respectively.

is constructed as shown in Fig. 1h. Meanwhile, TEM results show that the Ru nanoparticles prepared by liquid phase chemical method used for prepare Ru/C are evenly distributed, and the particle size is concentrated between 3 and 5 nm (Fig. S4a and b). The spacing of adjacent fringes is mainly 0.208, 0.218 and 0.280 nm (Fig. S4c and d), which is indexed to the (101), (002), and (100) crystalline plane of hcp Ru nanoparticles in Ru/C. By comparison, it can be found that the crystal plane spacing of hcp Ru particles in V-S-Ru/C and S-Ru/C is smaller than that of Ru/C, which means the existence of compression stress.

The structure of V-S-Ru/C and S-Ru/C were investigated by X-Ray Diffraction (XRD). In Fig. 2a, two distinct wide peaks located at $\sim 26.4^\circ$ and $\sim 44.4^\circ$ can be attributed to graphite carbon respectively (PDF#41-1487). Other diffraction peaks at $\sim 38.4^\circ$, 42.2° , 44.0° , 58.3° , and 69.4° coincided well with the planes of (100), (002), (101), (102), and (110) of the hcp Ru crystal (PDF#88-1734). Compared with S-Ru/C, the diffraction peak intensity attributed to hcp Ru in V-S-Ru/C is significantly smaller, which means that the size of Ru nanoparticles is smaller and the distribution is more uniform [40]. In addition, the local XRD peaks corresponding to Ru shifted slightly to the higher degree, indicating that there was slight lattice compression of Ru particles in both S-Ru/C and V-S-Ru/C. Further structural analysis of V-S-Ru/C and S-Ru/C was conducted by X-ray Photoelectron Spectroscopy (XPS). As shown in Fig. 2b, four peaks for Ru $3d_{5/2}$ (~ 280.6 eV), sp^2 hybridized C (~ 284.8 eV), sp^3 hybridized C (~ 285.9 eV), Ru $3d_{3/2}$ (~ 284.6 eV), can be identified respectively [19,32]. Chemical states of Ru in V-S-Ru/C and S-Ru/C were revealed by the Ru 3p spectra to avoid C 1 s interference. As shown in Fig. 2c, two couples of fitted peaks corresponding to Ru^0 (461.9/484.3 eV) and Ru^{3+} (464.5/487.2 eV) were observed [59]. By comparison, it can be found that the valence state of Ru in V-S-Ru/C is slightly higher than that in S-Ru/C (Fig. 2c and Table S1), this may be due to the vacancy structure and smaller size lead to more exposure of metal sites and higher surface energy [51,60], and this may also implies electron transfer from Ru to carbon substrate due to the strong interaction between support and metal Ru nanoparticles. Moreover, the BET surface areas of V-S-Ru/C and S-Ru/C were 142.454 and 90.095 m^2/g , respectively, indicating that the V-S-Ru/C obtained by PVP possessed a large specific surface area, which is in line with TEM observation results.

Synchrotron radiation-based X-ray absorption fine structure (XAFS) was then carried out to study the local configuration of V-S-Ru/C by using Ru foil and RuO_2 as counterparts. As shown in Fig. 2d, the adsorption edge of V-S-Ru/C is close to that of Ru foil, indicating the metallic characteristic of V-S-Ru/C. Besides, the shape of X-ray absorption near-edge structure (XANES) spectra of Ru V-S-Ru/C is slightly different from that of Ru foil, which may be because of the different local coordination environments [51]. Hence, the k^3 -weighted Fourier-transformed EXAFS (FT-EXAFS) spectra were further recorded to reveal the local geometric structure of the Ru samples. As illustrated in Fig. 2e, two separated peaks located at 1.50 and 2.30 Å in the FT-EXAFS curve of V-S-Ru/C could be observed, which are corresponding to the Ru-C and Ru-Ru bonds, respectively. It is observed that the bond length of Ru-Ru in V-S-Ru/C is shortened compared with that in Ru foil (2.42 Å), which may be caused by lattice compression [51]. The fitting results revealed that the coordination number of the Ru-Ru bond in V-S-Ru/C is 5.0 (Fig. 2f and Table S2), which is lower than that of Ru foil (i.e. 12). In addition, the Ru-C bond with an average coordination number of 2.3 can also be observed due to the interaction between Ru atom and with a graphitized carbon layer [60]. The decreased Ru-Ru coordination further confirms that rich structural defects may exist in the V-S-Ru/C, following the AC-HAADF-STEM results mentioned before. Moreover, the wavelet transforms (WTs) of Ru K-edge EXAFS were also carried out to explore the local structure of V-S-Ru/C (Fig. 2g-i). The WT maximum intensity for V-S-Ru/C is 8.62 \AA^{-1} , while the WT maximum intensity for Ru foil is 10.00 \AA^{-1} . The shift of the WT maximum is probably caused by the structural defects of V-S-Ru/C.

3.3. The HER performance

Electrochemical HER of Ru-based catalysts annealed with various methods were evaluated in 1 M KOH aqueous solution. To be accurate, the reference Hg/HgO electrode was calibrated against RHE in 1 M KOH media with H_2 -saturated before all tests (Fig. S5) [28]. In Fig. 3a, the measured LSV curves with 90% iR compensation showed that V-S-Ru/C achieved a current density of 10 mA/cm^2 with an overpotential 21 mV versus RHE, which was much lower than S-Ru/C (54 mV). The HER performance of Ru/C has been declining with the increase of testing times, so no subsequent analysis will be given for its instability and poor activity. Furthermore, the mass activity shows that V-S-Ru/C has obvious advantages over S-Ru/C (Fig. S7a). Tafel curves in Fig. 3b were derived from LSV curves in Fig. 3a. The V-S-Ru/C obtained an ultralow Tafel slope of 31.08 mV/dec, far lower than S-Ru/C (68.35 mV/dec). The lower the Tafel slope, the faster the current density increases with the overpotential [19]. To further explore the nature of the observed high activity of V-S-Ru/C, the C_{dl} were measured in Fig. 3c (12.45 mF/cm^2 for V-S-Ru/C and 4.03 mF/cm^2 for S-Ru/C). The values of C_{dl} are obtained by data processing of cyclic voltammetry at different scanning speeds, as shown in Fig. S6a and b. The results show that the ECSA of the V-S-Ru/C catalyst was nearly 3.1 times that of S-Ru/C (21.99 cm^2 for V-S-Ru/C and 7.12 mF/cm^2 for S-Ru/C), but its current density at 100 mV overpotential was nearly 6.5 times that of S-Ru/C (-188.4 mA/cm^2 for V-S-Ru/C and -29.2 mA/cm^2 for S-Ru/C). Moreover, the ECSA-normalized LSV curves of V-S-Ru/C and S-Ru/C were also given in Fig. S7b. The above data evidenced that the better performance of V-S-Ru/C was not only owing to the more active sites, but also because of the high activity of each active site. The electrochemical impedance patterns of V-S-Ru/C and S-Ru/C were shown in Fig. 3d, which can be fitted by the equivalent circuit (inset of Fig. 3d). As it can be seen from Bode plots (Fig. S7c and d) that there is only one phase angle peak between high frequency and low frequency, so the equivalent circuit fitting of one time is reasonable. The fitted electrochemical data were summarized in Table S3. The charge transfer impedance of V-S-Ru/C was much smaller than S-Ru/C, which implies its faster charge transfer kinetics and electron transport in HER [61,62]. The long-term stability test of V-S-Ru/C was shown in Fig. 3e, which confirms the as-synthesized V-S-Ru/C maintains its high HER activity and shows good stability. The LSV curves before and after 10000 circles CV were illustrated in the inset of Fig. 3e, showing similar results. In order to exclude the slight degradation of catalyst was due to the loss of activity during the long-time HER test on GCE. The catalyst was loaded on carbon paper for HER test for a long-time constant current test also. It can be seen that the performance of the catalyst activity hardly changed from the floating voltage changes in the constant current test or LSV curves before and after the constant current test (Fig. S8c and d). From the TEM images of the catalyst before and after the constant current test, it can be observed that no significant changes in the particles have been observed (Fig. S8a and b). Moreover, a comparison of the optimal catalyst to commercial 20 wt% Pt/C was also given, as shown in Fig. 3a (inset). Compared with commercial 20 wt% Pt/C, V-S-Ru/C catalyst showed 2.6 times of area current density at 100 mV overpotential. After mass normalization, the V-S-Ru/C catalyst showed up to 35.6 times more mass activity than commercial 20 wt% Pt/C at 100 mV overpotential ($19,949.51 \text{ mA/mg}$ for V-S-Ru/C and 560.42 mA/mg for 20 wt% Pt/C respectively). To emphasize the high performance of V-S-Ru/C, a brief summarization of the overpotential required at 10 mA/cm^2 and Ru mass loading on the electrode for various Ru-based HER catalysts in 1.0 M KOH was shown in Fig. 3f. There was no doubt that V-S-Ru/C catalyst exhibits very good performance at low mass loading compared to many other works.

3.4. The HOR performance

The HOR performance of the V-S-Ru/C commercialized 20 wt% Pt/C and S-Ru/C catalysts were examined in an H_2 -saturated 0.1 M KOH

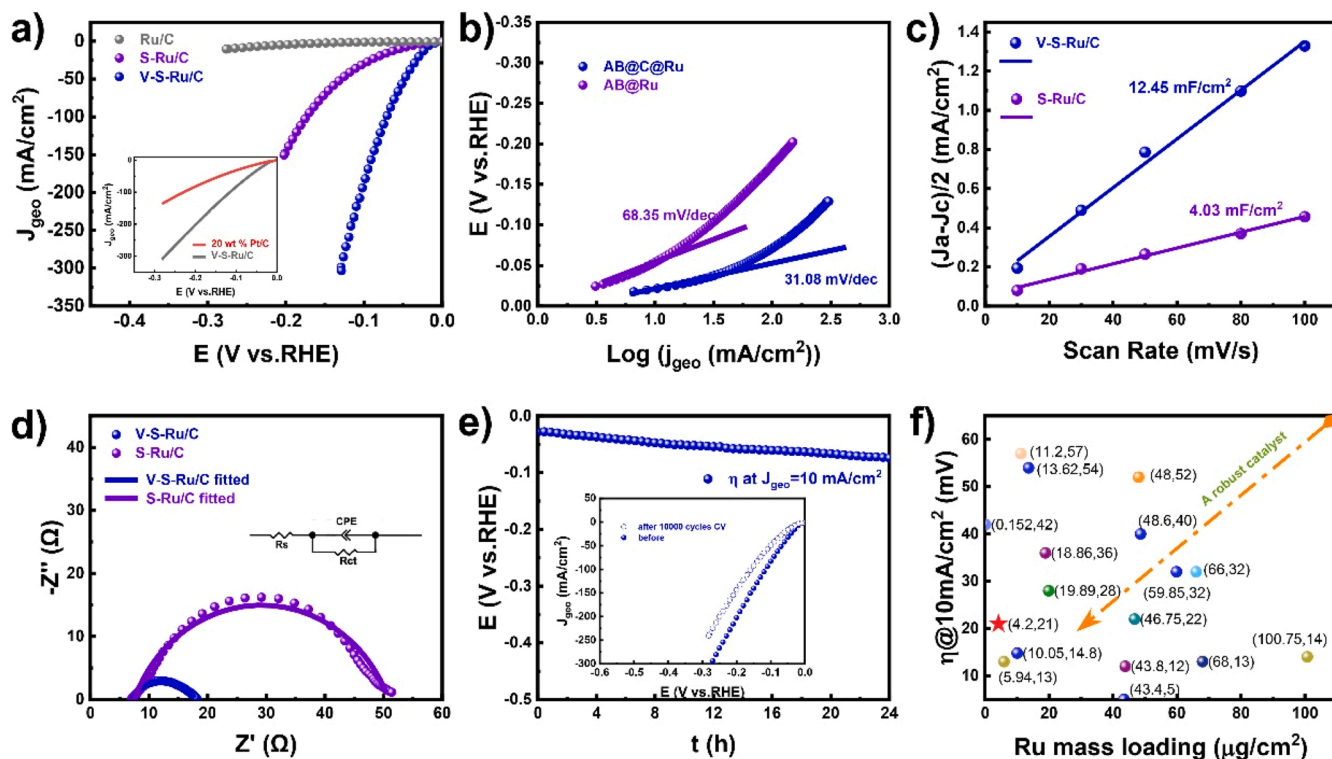


Fig. 3. (a) LSV curves (inset: LSV curves of V-S-Ru/C and 20 wt% Pt/C without iR corrected) and (b) corresponding Tafel plots of Ru-based catalysts. (c) C_{dl} values of the Ru-based catalysts. (d) Electrochemical impedance diagrams of V-S-Ru/C and S-Ru/C catalysts, respectively (inset: equivalent circuit model). (e) Stability test at 10 mA/cm² (inset: LSV curves before and after 10000 cycles CV). (f) Comparison of the overpotential which was required at 10 mA/cm² and Ru mass loading on the electrode (see Table S4 for detailed data).

electrolyte. As it can be seen from Fig. 4a, not only the activity of V-S-Ru/C is higher than that of S-Ru/C under the whole potential range but also HOR activity of S-Ru/C decreases rapidly while V-S-Ru/C continues to maintain a high activity when the potential exceeds ~ 0.15 V. Similar to the test results of HER, the HOR performance of the Ru/C catalyst also decreases with the increase in test times, which means that it is unstable. Therefore, the Ru/C test will not be conducted and analyzed for the subsequent relevant tests of the HOR catalyst evaluation indicators. By comparing the LSV curves of the V-S-Ru/C catalyst in 0.1 M KOH solution saturated with H_2 and N_2 , it can be confirmed that the collected anodic current was due to the HOR (see Fig. S9a). According to the reported work, when the potential is too high, the surface of Ru nanoparticles will lose the HOR active site due to the generation of oxygen-active species, resulting in the rapid deterioration of HOR performance [52]. The catalytic behavior of the V-S-Ru/C catalyst, however, was similar to that of commercial Pt/C catalyst (inset of Fig. S4a), and this means that the catalytic behavior of the V-S-Ru/C catalyst was fully altered by the strong interaction between carbon support and Ru nanoparticles. The high activity of V-S-Ru/C was due to its small particle size, lattice stress and a certain degree of defective structure [63]. The exchange current density (j_0) of the synthesized catalysts can be obtained from linear fitting of micro-polarization regions (i.e., from -10 mV to 10 mV) (Fig. 4b and Table S5), through the simplified Butler-Volmer equation [2,28], $j_0 = (j/\eta)(RT/F)$, in which R equals the universal gas constant, T equals the temperature in the Kelvin scale, F equals Faraday's constant, j equals the measured current density, and η equals the applied overpotential. The j_0 for V-S-Ru/C was 1.43 mA/cm^2 , which was 2.3 times that of S-Ru/C. After mass normalization of the exchange current densities ($j_{0,m}$) of V-S-Ru/C and S-Ru/C, it could be found that the $j_{0,m}$ of V-S-Ru/C (340.18 mA/mg) was 2.6 times that of S-Ru/C (129.97 mA/mg). In addition, the mass activity of V-S-Ru/C was significantly higher than that of S-Ru/C (Fig. S9b). By comparing the position of the desorption peak of underpotential deposited hydrogen

(H_{UPD}), V-S-Ru/C was 48 mV lower than S-Ru/C (Fig. S9c), which means V-S-Ru/C has a lower H binding energy [1]. In addition, desorption peak area of H_{UPD} showed that V-S-Ru/C was 6.6 times larger than S-Ru/C (Fig. S9c), indicating that V-S-Ru/C has more active sites than S-Ru/C. An accelerated durability test was conducted by performing 1000 cycles of CV scans from -0.011 – 0.089 V (vs. RHE) at a scan rate of 100 mV/s . LSV curves showed that V-S-Ru/C experienced only a negligible decrease in HOR activity after this process (Fig. 4c). To further verify the HOR catalytic stability of the catalyst, the V-S-Ru/C catalyst was dripped onto carbon paper and then subjected to 4 times of 10000 s constant potential (at 0.189 V vs. RHE) test. Fig. 4d shows LSV curves before and after each constant potential test of the catalyst. Fig. 4e shows the Amperometric i - t curves for each constant potential test. In general, the stability of the catalyst was good, but the HOR activity at high potential was also moderately decreased, indicating that moderate oxidation does occur on the surface of Ru nanoparticles [52,63]. From the comparison of $j_{0,m}$ and j_m values at 50 mV overpotential (j_m at $\eta = 0.05 \text{ V}$) in Fig. 4f, it can be seen that V-S-Ru/C has higher activity than S-Ru/C. In addition, the j_m at $\eta = 0.05 \text{ V}$ value of V-S-Ru/C was 7.2 times that of commercial 20 wt% Pt/C, showing ultra-high HOR mass activity (Fig. S9d). In addition, the optimization of the low-temperature section of synthesis V-S-Ru/C (Fig. S9e) and the use of one-step high-temperature thermal reduction Fig. S9f were also explored. The results show that the catalytic activity was the highest when the temperature was 300°C in low temperatures and 800°C at high temperatures. Finally, by comparing the HOR activity of V-S-Ru/C with that of other precious metals (especially Ru) reported recently (Table S6), it can be found that the HOR activity of V-S-Ru/C was excellent. Furthermore, the hydroxide exchange membrane fuel cell (HEMFC) composed of V-S-Ru/C as an anodic catalyst, and 40 wt% Pt/C as a cathode shows a peak power density of 567 mW/cm^2 (Fig. 4g and h), better than those of the RuNi/NC (540 mW/cm^2) [64], Ru/C (250 mW/cm^2) [65], and Ni- H_2 - NH_3 (488 mW/cm^2) [12].

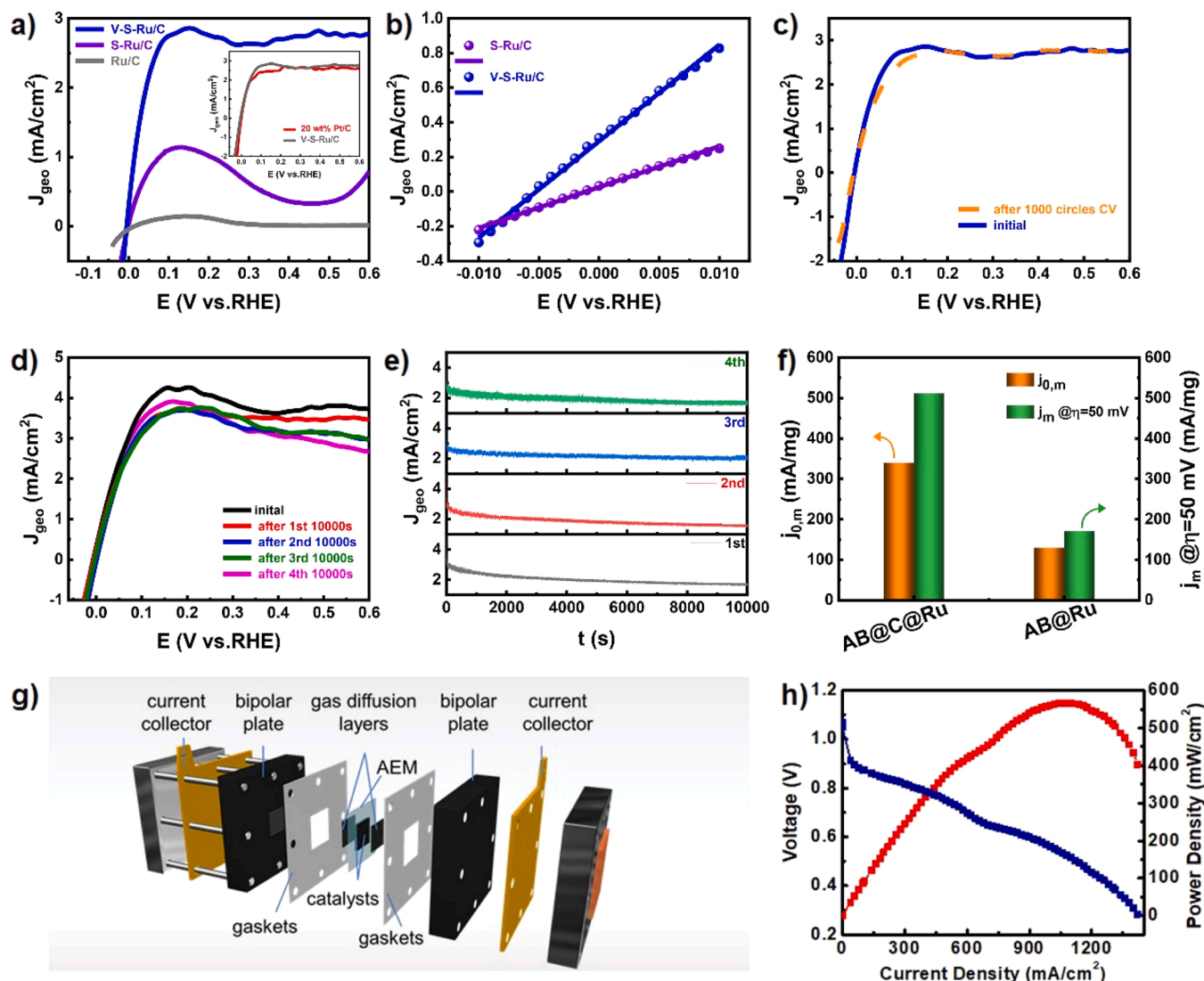


Fig. 4. (a) LSV curves (inset: LSV curves of V-S-Ru/C and 20 wt% Pt/C) and (b) Micro-polarization region (-10 to 10 mV) of Ru-based catalysts. (c) LSV curves before and after 1000 cycles CV of V-S-Ru/C. (d) LSV curves of V-S-Ru/C catalyst dropped on carbon paper ($1\text{ cm} \times 1\text{ cm}$) after different times of 10000 s constant potential test. (e) 4 times of 10000 s constant potential test curves. (f) Comparison of $j_{0,m}$ and j_m at $\eta = 0.05$ V for V-S-Ru/C and S-Ru/C catalysts. (g) Structure schematic diagram of fuel cell. (h) Cell performance of the HEMFC using V-S-Ru/C as anode catalysts with a catalyst loading of $0.2\text{ mg}_{\text{Ru}}/\text{cm}^2$ and 40% Pt/C as cathode catalyst with a loading of $0.4\text{ mg}_{\text{Pt}}/\text{cm}^2$, fed with 100% humidified H_2 and O_2 at a flow rate of $500\text{ mL}/\text{min}$ with a backpressure of 0.2 MPa and operated at 80°C .

3.5. DFT calculation

The atomic model of the bulk Ru and C structures was depicted in Fig. S10. According to the XRD data, the lattice constants of bulk C were $a = b = 2.47\text{ \AA}$, $c = 6.72\text{ \AA}$, and those of bulk Ru were $a = b = 2.70\text{ \AA}$, $c = 4.28\text{ \AA}$, with an angle of $90.0^\circ \times 90.0^\circ \times 120.0^\circ$ and P6/MMM space group. The HRTEM observation shown in Fig. 1 was comparable with the heterojunction model that was built using the C (001) plane and Ru (001) plane, which has a small planar mismatch of around 0.80%. In Fig. S10, several interface models were built utilizing various atom counts ranging from 72 to 190 (Fig. S10d-g). The model with 72 atoms was thought to be appropriate and expected to simulate our experimentally fabricated samples when computing time and resources were taken into account. The EXAFS finding indicates that the coordination number of Ru was substantially less than that of the ideal crystal structure. Therefore, the defective Ru/C was created by withdrawing the Ru atom from the catalytic surface. To analyze the observed difference and the origin of V-S-Ru/C as a prospective HER and HOR catalyst, DFT calculations were carried out (Fig. 5). Most researchers agree that HER

proceeds forward via the Volmer-Heyrovsky or Volmer-Tafel steps. A popular microkinetic model for selecting the ideal HER catalyst in an acid solution is the Gibbs free energy model for hydrogen adsorption (G_{H^*}). It often works better as a catalyst when the value of G_{H^*} is near thermoneutral. With Ru as the active site, the computed values of Ru/C, S-Ru/C and V-S-Ru/C were -1.04 eV , 1.32 eV and -0.48 eV , respectively (Figs. 5a and S11). However, the apparent HER activity in alkaline solutions cannot be qualitatively confirmed by the G_{H^*} value on its own. Furthermore, it is necessary to provide a thorough comprehension of the respective reaction paths of the Ru-based electrocatalysts. It is important to consider the thermodynamic behavior of water dissociation into H and OH species.

The activity of the three electrocatalysts shown in Figs. 5b and S12 were described using the Gibbs free energy of reaction pathways on Ru/C, S-Ru/C and V-S-Ru/C (001). The typical HER process in alkaline media involves the initial adsorption of water on active sites (H_2O^*), co-adsorption of $\text{H}^* + \text{OH}^*$, and the formation and release of H^* to H_2 gas. HOR starts with hydrogen adsorption on the surface and forms the H^* , followed by the co-adsorption of $\text{H}^* + \text{OH}^*$ and the release of H_2O .

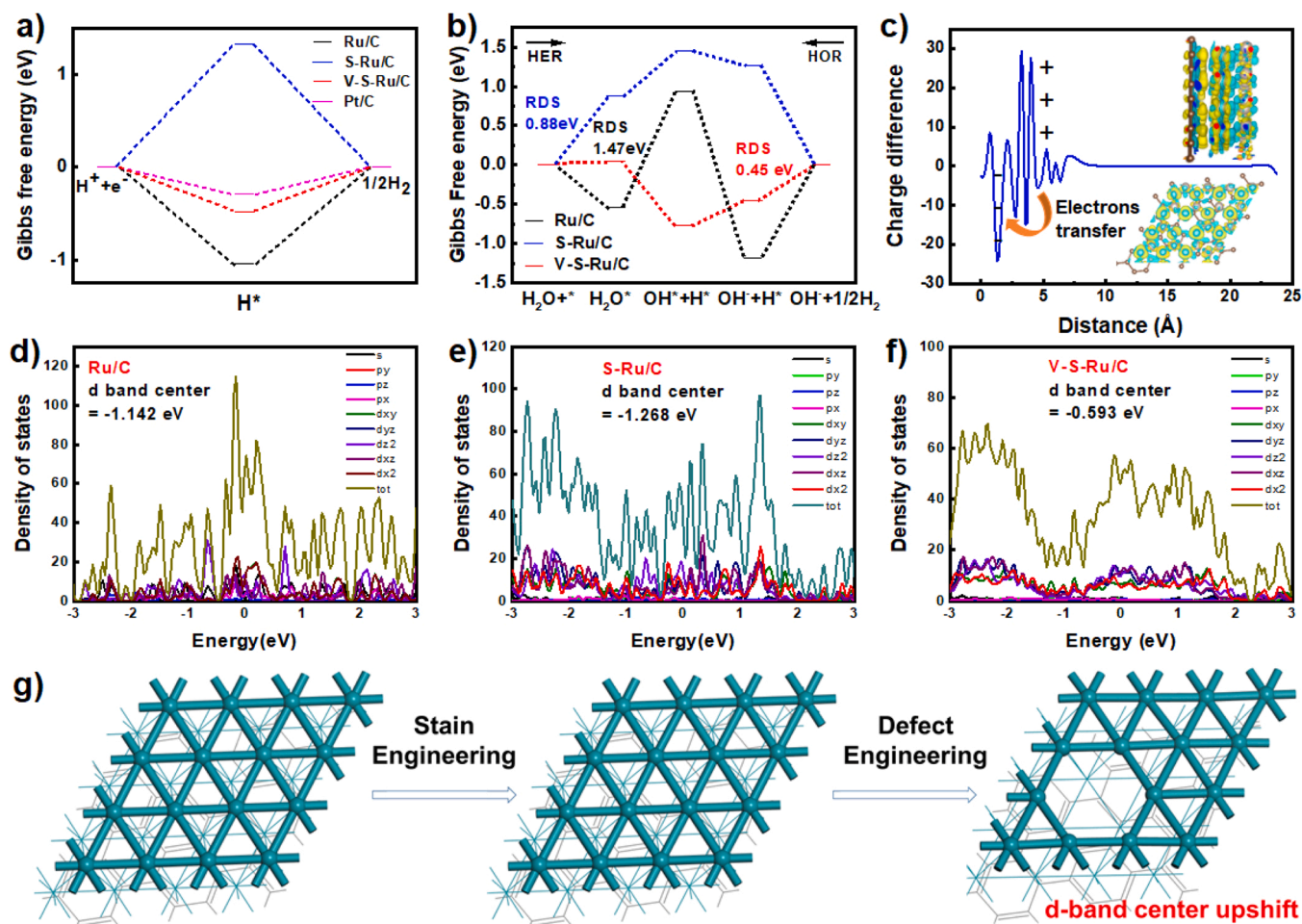


Fig. 5. (a) The calculated free-energy diagram of the HER at the equilibrium potential for Ru/C, S-Ru/C, V-S-Ru/C, and Pt/C. (b) Reaction pathways of Ru/C, S-Ru/C, and V-S-Ru/C 001 for the alkaline HER and HOR. (c) The charge density difference of the V-S-Ru/C with the yellow area representing electron accumulation and the cyan part means electron depletion. The density of states of (d) Ru/C, (e) S-Ru/C and (f) V-S-Ru/C with d band center. (g) The illustration of Ru/C, S-Ru/C and V-S-Ru/C with configurations.

According to the free energy diagram on the (001) surface of V-S-Ru/C, the increased adsorption ability of H^* intermediates might accelerate the kinetics of H adsorption. Additionally, the adsorption energy of H_2O on S-Ru/C was greater (0.88 eV) than that on V-S-Ru/C (0.048 eV). H_2O adsorption at an energy of 0.88 eV was the rate-determining step (RDS) of S-Ru/C. Through incorporating defects into the S-Ru/C (i.e. V-S-Ru/C), the free energy for the RDS, which was the H_2 -desorption step, was decreased to 0.45 eV. While for the Ru/C, the RDS was the H_2O -splitting step with the free energy of 1.47 eV. Among these electrocatalysts, the reduced RDS for V-S-Ru/C shows the highest enhancement in water dissociation performance in alkaline solutions. The electrostatic potential along the Z axis was estimated to evaluate the inherent potential of the V-S-Ru/C, as illustrated in Fig. S13. Fig. S13a-d shows the calculation of the potential of pure C (001) and pure Ru (001). The average potential on the C side of the heterojunction was larger than that on the Ru side after the potential of the S-Ru/C and V-S-Ru/C were also calculated. The driving force also points in the direction of charge transfer, which was from Ru to C. As illustrated in Fig. 5c, the charge density difference indicates the interfacial charge transfer direction between C and Ru, and this was consistent with the observation of XPS results. The top and cross views of the optimized three-dimensional atomic model were shown in the insets. The cyan area represents charge depletion on the Ru part of the defect interface between C and Ru, and the yellow region represents charge accumulation on the C side. The corresponding curve depicts the charge transfer from Ru to C, which

is presented with positive charge density on the Ru part and negative charge density on the C part. Additionally, the Bader charges of Ru atoms were carried out to provide a quantitative comparison of the electron transfer. The results indicate that S-Ru/C distributes 0.80 electrons to the H atom and that V-S-Ru/C donates 0.65 electrons to H (Fig. S14), which suggests that there is less electron transfer between neighbouring Ru atoms and the adsorption of H.

Fig. 5d-f depicts the state density of the Ru/C, S-Ru/C, and V-S-Ru/C, with the Ru atoms whose d orbitals contribute more to the outermost orbit. Higher conductivity is the result of improved electrochemical reactions in this scenario. S-Ru/C has a d-band center of -1.268 eV, while V-S-Ru/C has a value of -0.593 eV. H_2 adsorption is facilitated by the upshift of the d-band center. The decrease in the filling of as-hybridized antibonding orbitals ($(d-\sigma)^*$) and the stabilization of the interaction between the catalyst surface and the adsorbates would result in the upshift of the d-band center, and thermodynamically boosting the binding capacity of V-S-Ru/C sites with intermediates for better HER and HOR activity. Fig. 5g-h depicts the adjustment of d-band center on Ru/C, S-Ru/C and V-S-Ru/C with configurations. The findings of theoretical calculations show how the defect engineering and strain engineering synergistically optimize the Gibbs free energy for the adsorption of H, OH, and $H + OH$, and leading to the enhanced HER and HOR performance on the V-S-Ru/C.

4. Conclusion

In summary, we develop efficient Ru-based electro-catalyst through the jointly regulation of defect engineering and stress engineering to realize excellent HER and HOR activity, which is different from the previous way of single factor adjustment. The heterojunction of Ru nanoparticles and twisted graphitized carbon was formed through pyrolysis of PVP-protected Ru complex at high temperatures. Through electron microscopic and spectroscopic characterization, the obtained ultrafine Ru nanoparticles are uniform (~ 2.5 nm) in average diameter and contain some vacant or unoccupied sites. The twisted graphitized carbon layer exerts compressive stress on Ru nanoparticles, resulting in lattice distortion. Thereby the d-band center upshifts of this Ru/C heterojunction with compressive stress and vacancy, and the active Ru sites show advantages in the generation and adsorption of intermediates in the elementary steps of HER and HOR. This V-S-Ru/C heterojunction has excellent HER activity with overpotentials of 21 mV to deliver 10 mA/cm² in alkaline media, and the mass activity is 35.6 times that of commercial 20% Pt/C in 100 mA/cm². The V-S-Ru/C could also achieve 7.2 times the mass activity of commercial 20% Pt/C for HOR and has good oxidation resistance in the high potential range. The catalytic activity of Ru/C containing only compressive stress obtained by pyrolysis of un-protected Ru complex and common Ru/C obtained by impregnation method decreased significantly, which proved the effectiveness of strain engineering and defect engineering in regulating the electronic structure of Ru nanoparticles.

CRediT authorship contribution statement

Qikang Wu: Methodology, Validation, Formal analysis, Investigation, Data curation, Writing – original draft. **Wenjuan Yang, Xingdong Wang, Wei Zhu:** Experimental measurements. **Shanshan Lv, Yan Zhou, Taiyu Chen:** Data collection and processing, Discussion. **Shaohuan Liu, Wanying Li:** Discussion. **Zheng Chen:** Supervision, Conceptualization.

Declaration of Competing Interest

The authors declare that they have no known competing financial interests or personal relationships that could have appeared to influence the work reported in this paper.

Data availability

No data was used for the research described in the article.

Acknowledgements

This work was supported by the National Natural Science Foundation of China (21866032), the Key Research and Development Project of Anhui Province (2022a05020048), and the Open Project of Anhui Province Key Laboratory for Degradation and Monitoring of Pollution of the Environment (FSKFKT007D). We would like to express our gratitude to Prof. Jing Xia in the Technical Institute of Physics and Chemistry CAS for his help in the AC-HAADF-STEM.

Appendix A. Supporting information

Supplementary data associated with this article can be found in the online version at [doi:10.1016/j.apcatb.2023.122896](https://doi.org/10.1016/j.apcatb.2023.122896).

References

- [1] Z.C. Yao, T. Tang, Z. Jiang, L. Wang, J.S. Hu, L.J. Wan, Electrocatalytic hydrogen oxidation in alkaline media: from mechanistic insights to catalyst design, *ACS Nano* 16 (2022) 5153–5158.
- [2] X. Wang, J. Fang, X. Liu, D. Wei, Y. Yin, H. Wei, J. Zhang, Y. Zhang, X. Zhang, W. Zhu, Z. Zhuang, Nitrogen-doped carbon as selectively permeable layer to enhance the anti-poisoning ability of hydrogen oxidation reaction catalysts for hydroxide exchange membrane fuel cells, *Appl. Catal. B-Environ.* 327 (2023), 122442.
- [3] Y. Duan, Z.Y. Yu, L. Yang, L.R. Zheng, C.T. Zhang, X.T. Yang, F.Y. Gao, X.L. Zhang, X. Yu, R. Liu, H.H. Ding, C. Gu, X.S. Zheng, L. Shi, J. Jiang, J.F. Zhu, M.R. Gao, S. H. Yu, Bimetallic nickel-molybdenum/tungsten nanoalloys for high-efficiency hydrogen oxidation catalysis in alkaline electrolytes, *Nat. Commun.* 11 (2020) 4789.
- [4] K. Jiang, Z. Liu, Y.R. Lu, M. Wang, D. Chen, L. Cai, T.S. Chan, P. Liu, A. Pan, Y. Tan, Rapid melt-quenching enables general synthesis of high-loading single-atom catalysts with bicontinuous nanoporous structure, *Adv. Mater.* 35 (2023), e2207850.
- [5] A. Karmakar, K. Karthick, S.S. Sankar, S. Kumaravel, R. Madhu, K. Bera, H. N. Dhandapani, S. Nagappan, P. Murugan, S. Kundu, Stabilization of ruthenium nanoparticles over NiV-LDH surface for enhanced electrochemical water splitting: an oxygen vacancy approach, *J. Mater. Chem. A* 10 (2022) 3618–3632.
- [6] W. Luo, Y. Wang, C. Cheng, Ru-based electrocatalysts for hydrogen evolution reaction: Recent research advances and perspectives, *Mater. Today Phys.* 15 (2020), 100274.
- [7] B. Zhang, G. Zhao, B. Zhang, L. Xia, Y. Jiang, T. Ma, M. Gao, W. Sun, H. Pan, Lattice-Confined Ir Clusters on Pd Nanosheets with Charge Redistribution for the Hydrogen Oxidation Reaction under Alkaline Conditions, *Adv. Mater.* 33 (2021), e2105400.
- [8] L. Su, D. Gong, Y. Jin, D. Wu, W. Luo, Recent advances in alkaline hydrogen oxidation reaction, *J. Energy Chem.* 66 (2022) 107–122.
- [9] Z. Kang, H. Wang, Y. Liu, J. Mo, M. Wang, J. Li, X. Tian, Exploring and understanding the internal voltage losses through catalyst layers in proton exchange membrane water electrolysis devices, *Appl. Energy* 317 (2022), 119213.
- [10] Y. Liu, X. Li, Q. Zhang, W. Li, Y. Xie, H. Liu, L. Shang, Z. Liu, Z. Chen, L. Gu, Z. Tang, T. Zhang, S. Lu, A General Route to Prepare Low-Ruthenium-Content Bimetallic Electrocatalysts for pH-Universal Hydrogen Evolution Reaction by Using Carbon Quantum Dots, *Angew. Chem. Int. Ed.* 59 (2020) 1718–1726.
- [11] J. Mao, C.T. He, J. Pei, W. Chen, D. He, Y. He, Z. Zhuang, C. Chen, Q. Peng, D. Wang, Y. Li, Accelerating water dissociation kinetics by isolating cobalt atoms into ruthenium lattice, *Nat. Commun.* 9 (2018) 4958.
- [12] W. Ni, T. Wang, F. H  rogu  l, A. Krammer, S. Lee, L. Yao, A. Sch  ler, J. S. L  tzbacher, Y. Yan, X. Hu, An efficient nickel hydrogen oxidation catalyst for hydroxide exchange membrane fuel cells, *Nat. Mater.* 21 (2022) 804–810.
- [13] S. Ajmal, H.T.D. Bui, V.Q. Bui, T. Yang, X. Shao, A. Kumar, S.-G. Kim, H. Lee, Accelerating water reduction towards hydrogen generation via cluster size adjustment in Ru-incorporated carbon nitride, *Chem. Eng. J.* 429 (2022), 132282.
- [14] Y. Li, J. Abbott, Y. Sun, J. Sun, Y. Du, X. Han, G. Wu, P. Xu, Ru nano assembly catalysts for hydrogen evolution and oxidation reactions in electrolytes at various pH values, *Appl. Catal. B-Environ.* 258 (2019), 117952.
- [15] J. Wang, Y. Zhao, B.P. Setzler, S. Rojas-Carbonell, C. Ben Yehuda, A. Amel, M. Page, L. Wang, K. Hu, L. Shi, S. Gottesfeld, B. Xu, Y. Yan, Poly(aryl piperidinium) membranes and ionomers for hydroxide exchange membrane fuel cells, *Nat. Energy* 4 (2019) 392–398.
- [16] D. Merki, H. Vrubel, L. Rovelli, S. Fierro, X. Hu, Fe, Co, and Ni ions promote the catalytic activity of amorphous molybdenum sulfide films for hydrogen evolution, *Chem. Sci.* 3 (2012) 2515–2525.
- [17] A.P. Murthy, J. Theerthagiri, J. Madhavan, K. Murugan, Highly active MoS₂/carbon electrocatalysts for the hydrogen evolution reaction—insight into the effect of the internal resistance and roughness factor on the Tafel slope, *Phys. Chem. Chem. Phys.* 19 (2017) 1988.
- [18] J. Wang, X. Dong, J. Liu, W. Li, L.T. R  ling, J. Xiao, L. Jiang, Ultrafine nickel nanoparticles encapsulated in n-doped carbon promoting hydrogen oxidation reaction in alkaline media, *ACS Catal.* 11 (2021) 7422–7428.
- [19] Q. He, Y. Zhou, H. Shou, X. Wang, P. Zhang, W. Xu, S. Qiao, C. Wu, H. Liu, D. Liu, S. Chen, R. Long, Z. Qi, X. Wu, L. Song, Synergic reaction kinetics over adjacent ruthenium sites for superb hydrogen generation in alkaline media, *Adv. Mater.* 34 (2022), 2110604.
- [20] T. Li, X. Zhang, Y. Chen, L. Zhong, S. Li, P. Zhang, C. Zhao, Boosting the water dissociation kinetics via charge redistribution of ruthenium decorated on S, N-codoped, Carbon, *J. Mater. Chem. A* 9 (2021) 16967–16973.
- [21] Y. Zheng, Y. Jiao, Y. Zhu, L.H. Li, Y. Han, Y. Chen, M. Jaroniec, S.Z. Qiao, High electrocatalytic hydrogen evolution activity of an anomalous ruthenium catalyst, *J. Am. Chem. Soc.* 138 (2016) 16174–16181.
- [22] P. Li, X. Duan, S. Wang, L. Zheng, Y. Li, H. Duan, Y. Kuang, X. Sun, Amorphous Ruthenium-Sulfide with Isolated Catalytic Sites for Pt-Like Electrocatalytic Hydrogen Production Over Whole pH Range, *Small* 15 (2019), 1904043.
- [23] T. Zhao, Y. Hu, M. Gong, R. Lin, S. Deng, Y. Lu, X. Liu, Y. Chen, T. Shen, Y. Hu, L. Han, H. Xin, S. Chen, D. Wang, Electronic structure and oxophilicity optimization of mono-layer Pt for efficient electrocatalysis, *Nano Energy* 74 (2020), 104877.
- [24] L. Su, D. Gong, N. Yao, Y. Li, Z. Li, W. Luo, Modification of the Intermediate Binding Energies on Ni/Ni₃N Heterostructure for Enhanced Alkaline Hydrogen Oxidation Reaction, *Adv. Funct. Mater.* 31 (2021), 2106156.
- [25] J. Chen, M. Qin, S. Ma, R. Fan, X. Zheng, S. Mao, C. Chen, Y. Wang, Rational construction of Pt/PtTe_x interface with optimal intermediate adsorption energy for efficient hydrogen evolution reaction, *Appl. Catal. B-Environ.* 299 (2021), 120640.
- [26] Y. Chen, R. Ding, J. Li, J. Liu, Highly active atomically dispersed platinum-based electrocatalyst for hydrogen evolution reaction achieved by defect anchoring strategy, *Appl. Catal. B-Environ.* 301 (2022), 120830.

- [27] J. Peng, Y. Chen, K. Wang, Z. Tang, S. Chen, High-performance Ru-based electrocatalyst composed of Ru nanoparticles and Ru single atoms for hydrogen evolution reaction in alkaline solution, *Int. J. Hydrog. Energ.* 45 (2020) 18840–18849.
- [28] Y. Zhao, X. Wang, G. Cheng, W. Luo, Phosphorus-induced activation of ruthenium for boosting hydrogen oxidation and evolution electrocatalysis, *ACS Catal.* 10 (2020) 11751–11757.
- [29] J.-T. Ren, L. Chen, H.-Y. Wang, W.-W. Tian, X. Zhang, T.-Y. Ma, Z. Zhou, Z.-Y. Yuan, Inducing electronic asymmetry on Ru clusters to boost key reaction steps in basic hydrogen evolution, *Appl. Catal. B-Environ.* 327 (2023), 122466.
- [30] S.-Y. Bae, J. Mahmood, I.-Y. Jeon, J.-B. Baek, Recent advances in ruthenium-based electrocatalysts for the hydrogen evolution reaction, *Nanoscale Horiz.* 5 (2020) 43–56.
- [31] J. Zhang, Y. Gu, Y. Lu, C. Zhu, G. Liu, C. Wang, D. Sun, Y. Tang, H. Sun, Each performs its own functions: Nickel oxide supported ruthenium single-atoms and nanoclusters relay catalysis with multi-active sites for efficient alkaline hydrogen evolution reaction, *Appl. Catal. B-Environ.* 325 (2023), 122316.
- [32] L. Zhang, H. Jang, Y. Wang, Z. Li, W. Zhang, M.G. Kim, D. Yang, S. Liu, X. Liu, J. Cho, Exploring the dominant role of atomic- and nano-ruthenium as active sites for hydrogen evolution reaction in both acidic and alkaline media, *Adv. Sci.* 8 (2021), 2004516.
- [33] Y. Gao, Z. Chen, Y. Zhao, W. Yu, X. Jiang, M. He, Z. Li, T. Ma, Z. Wu, L. Wang, Facile synthesis of MoP-Ru₂P on porous N, P co-doped carbon for efficiently electrocatalytic hydrogen evolution reaction in full pH range, *Appl. Catal. B-Environ.* 303 (2022), 120879.
- [34] Z. Che, X. Lu, B. Cai, X. Xu, J. Bao, Y. Liu, Ligand-controlled synthesis of high density and ultra-small Ru nanoparticles with excellent electrocatalytic hydrogen evolution performance, *Nano Res.* 15 (2021) 1269–1275.
- [35] F. Zhu, J. Xue, L. Zeng, J. Shang, S. Lu, X. Cao, B.F. Abrahams, H. Gu, J. Lang, One-pot pyrolysis synthesis of highly active Ru/RuO_x nanoclusters for water splitting, *Nano Res.* 15 (2021) 1020–1026.
- [36] Y. Yang, D. Wu, R. Li, P. Rao, J. Li, P. Deng, J. Luo, W. Huang, Q. Chen, Z. Kang, Y. Shen, X. Tian, Engineering the strong metal support interaction of titanium nitride and ruthenium nanorods for effective hydrogen evolution reaction, *Appl. Catal. B-Environ.* 317 (2022), 121796.
- [37] A. Karmakar, S.S. Sankar, S. Kumaravel, R. Madhu, K.H. Mahmoud, Z.M. El-Bahy, S. Kundu, Ruthenium-Doping-Induced Amorphization of VS(4) Nanostructures with a Rich Sulfur Vacancy for Enhanced Hydrogen Evolution Reaction in a Neutral Electrolyte Medium, *Inorg. Chem.* 61 (2022) 1685–1696.
- [38] K. Jiang, M. Luo, Z. Liu, M. Peng, D. Chen, Y.R. Lu, T.S. Chan, F.M.F. de Groot, Y. Tan, Rational strain engineering of single-atom ruthenium on nanoporous MoS₂ for highly efficient hydrogen evolution, *Nat. Commun.* 12 (2021) 1687.
- [39] Q. Wu, M. Luo, J. Han, W. Peng, Y. Zhao, D. Chen, M. Peng, J. Liu, F.M.F. de Groot, Y. Tan, Identifying electrocatalytic sites of the nanoporous copper-ruthenium alloy for hydrogen evolution reaction in alkaline electrolyte, *ACS Energy Lett.* 5 (2019) 192–199.
- [40] Y. Li, L.A. Zhang, Y. Qin, F. Chu, Y. Kong, Y. Tao, Y. Li, Y. Bu, D. Ding, M. Liu, Crystallinity dependence of ruthenium nanocatalyst toward hydrogen evolution reaction, *ACS Catal.* 8 (2018) 5714–5720.
- [41] S.W. Sun, G.F. Wang, Y. Zhou, F.B. Wang, X.H. Xia, High-Performance Ru@C₄N Electro-catalyst for Hydrogen Evolution Reaction in Both Acidic and Alkaline Solutions, *ACS Appl. Mater. Interf.* 11 (2019) 19176–19182.
- [42] J. Cai, T. Chen, L. Cui, Q. Jia, M. Liu, R. Zheng, G. Yan, D. Wei, J. Liu, A three-dimensional and porous bi-nanospheres electrocatalytic system constructed by in situ generation of Ru nanoclusters inside and outside polydopamine nanoparticles for highly efficient hydrogen evolution reaction, *Int. J. Hydrog. Energ.* 45 (2020) 6592–6603.
- [43] A. Kuchipudi, S. Nagappan, A. Karmakar, G. Sreedhar, S. Kundu, Stabilization of Ru NPs over 3D LaCrO(3) Nanostructures for High-Performance HER Catalysts in Acidic Media, *Inorg. Chem.* 61 (2022) 19407–19416.
- [44] Z. Jiang, S. Song, X. Zheng, X. Liang, Z. Li, H. Gu, Z. Li, Y. Wang, S. Liu, W. Chen, D. Wang, Y. Li, Lattice Strain and Schottky Junction Dual Regulation Boosts Ultrafine Ruthenium Nanoparticles Anchored on a N-Modified Carbon Catalyst for H₂ Production, *J. Am. Chem. Soc.* 144 (2022) 19619–19626.
- [45] D.H. Kwon, M.S. Okyay, S.J. Kim, J.P. Jeon, H.J. Noh, N. Park, J. Mahmood, J. B. Baek, Ruthenium anchored on carbon nanotube electrocatalyst for hydrogen production with enhanced Faradaic efficiency, *Nat. Commun.* 11 (2020) 1278.
- [46] Y. Wang, W. Luo, H. Li, C. Cheng, Ultrafine Ru nanoclusters supported on N/S doped macroporous carbon spheres for efficient hydrogen evolution reaction, *Nanoscale Adv.* 3 (2021) 5068–5074.
- [47] M. Tan, Y. Wang, A. Taguchi, T. Abe, G. Yang, M. Wu, N. Tsubaki, Highly-dispersed Ru nanoparticles sputtered on graphene for hydrogen production, *Int. J. Hydrog. Energ.* 44 (2019) 7320–7325.
- [48] C. Wang, H. Shang, J. Li, Y. Wang, H. Xu, C. Wang, J. Guo, Y. Du, Ultralow Ru doping induced interface engineering in MOF derived ruthenium-cobalt oxide hollow nanobox for efficient water oxidation electrocatalysis, *Chem. Eng. J.* 420 (2021), 129805.
- [49] F. Li, G.F. Han, H.J. Noh, I. Ahmad, I.Y. Jeon, J.B. Baek, Mechanochemically Assisted Synthesis of a Ru Catalyst for Hydrogen Evolution with Performance Superior to Pt in Both Acidic and Alkaline Media, *Adv. Mater.* 30 (2018), 1803676.
- [50] L. Zeng, H. Peng, W. Liu, J. Yin, L. Xiao, J. Lu, L. Zhuang, Extraordinary activity of mesoporous carbon supported Ru toward the hydrogen oxidation reaction in alkaline media, *J. Power Sources* 461 (2020), 228147.
- [51] X. Yang, B. Ouyang, P. Shen, Y. Sun, Y. Yang, Y. Gao, E. Kan, C. Li, K. Xu, Y. Xie, Ru Colloidosome Catalysts for the Hydrogen Oxidation Reaction in Alkaline Media, *J. Am. Chem. Soc.* 144 (2022) 11138–11147.
- [52] Y. Zhou, Z. Xie, J. Jiang, J. Wang, X. Song, Q. He, W. Ding, Z. Wei, Lattice-confined Ru clusters with high CO tolerance and activity for the hydrogen oxidation reaction, *Nat. Catal.* 3 (2020) 454–462.
- [53] D. Strmcnik, M. Uchimura, C. Wang, R. Subbaraman, N. Danilovic, D. van der Vliet, A.P. Paulikas, V.R. Stamenkovic, N.M. Markovic, Improving the hydrogen oxidation reaction rate by promotion of hydroxyl adsorption, *Nat. Chem.* 5 (2013) 300–306.
- [54] S. John St., R.W. Atkinson, K.A. Unocic, R.R. Unocic, T.A. Zawodzinski, A. B. Papandrew, Platinum and palladium overlayers dramatically enhance the activity of ruthenium nanotubes for alkaline hydrogen oxidation, *ACS Catal.* 5 (2015) 7015–7023.
- [55] Z. Zhang, H. Liu, L. Ni, Z.-L. Zhao, H. Li, Scalable synthesis of hcp ruthenium-molybdenum nanoalloy as a robust bifunctional electrocatalyst for hydrogen evolution/oxidation, *J. Energy Chem.* 72 (2022) 176–185.
- [56] B. Zhang, B. Zhang, G. Zhao, J. Wang, D. Liu, Y. Chen, L. Xia, M. Gao, Y. Liu, W. Sun, H. Pan, Atomically dispersed chromium coordinated with hydroxyl clusters enabling efficient hydrogen oxidation on ruthenium, *Nat. Commun.* 13 (2022) 5894.
- [57] W. Yang, J. Li, X. Cui, C. Yang, Y. Liu, X. Zeng, Z. Zhang, Q. Zhang, Fine-tuning inverse metal-support interaction boosts electrochemical transformation of methanol into formaldehyde based on density functional theory, *Chin. Chem. Lett.* 32 (2021) 2489–2494.
- [58] W. Yang, Y. Zhu, J. Li, Z. Chen, F. Nosheen, Q. Zhang, Z. Zhang, Understanding the dehydrogenation mechanism over iron nanoparticles catalysts based on density functional theory, *Chin. Chem. Lett.* 32 (2021) 286–290.
- [59] Y. Feng, W. Feng, J. Wan, J. Chen, H. Wang, S. Li, T. Luo, Y. Hu, C. Yuan, L. Cao, L. Feng, J. Li, R. Wen, J. Huang, Spherical vs. planar: Steering the electronic communication between Ru nanoparticle and single atom to boost the electrocatalytic hydrogen evolution activity both in acid and alkaline, *Appl. Catal. B-Environ.* 307 (2022), 121193.
- [60] J. Yang, B. Chen, X. Liu, W. Liu, Z. Li, J. Dong, W. Chen, W. Yan, T. Yao, X. Duan, Y. Wu, Y. Li, Efficient and robust hydrogen evolution: phosphorus nitride imide nanotubes as supports for anchoring single ruthenium sites, *Angew. Chem. Int. Ed.* 57 (2018) 9495–9500.
- [61] Y. Gao, Y. Zhao, H. Liu, M. Shao, Z. Chen, T. Ma, Z. Wu, L. Wang, N. P-doped carbon supported ruthenium doped Rhenium phosphide with porous nanostructure for hydrogen evolution reaction using sustainable energies, *J. Colloid Interf. Sci.* 606 (2021) 1874–1881.
- [62] J. Li, C. Zhang, C. Zhang, H. Ma, Y. Yang, Z. Guo, Y. Wang, H. Ma, Electronic configuration of single ruthenium atom immobilized in urchin-like tungsten trioxide towards hydrazine oxidation-assisted hydrogen evolution under wide pH media, *Chem. Eng. J.* 430 (2022), 132953.
- [63] Y. Li, C. Yang, C. Ge, N. Yao, J. Yin, W. Jiang, H. Cong, G. Cheng, W. Luo, L. Zhuang, Electronic Modulation of Ru Nanosheet by d-d Orbital Coupling for Enhanced Hydrogen Oxidation Reaction in Alkaline Electrolytes, *Small* 18 (2022), e2202404.
- [64] L. Li Han, P. Ou, W. Liu, X. Wang, H. Wang, R. Zhang, C.-W. Pao, X. Liu, W.-F. Pong, J. Song, Z. Zhuang, M.V. Mirkin, J. Luo, H. Xin, Design of Ru-Ni diatomic sites for efficient alkaline hydrogen oxidation, *Sci. Adv.* 8 (2022) eabm3779.
- [65] J. Ohyama, T. Sato, A. Satsuma, High performance of Ru nanoparticles supported on carbon for anode electrocatalyst of alkaline anion exchange membrane fuel cell, *J. Power Sources* 225 (2013) 311–315.